IEEE Photonics Journal
An IEEE Photonics Society Publication

Open Access

Broadband High-Efficiency Electromagnetic Orbital Angular Momentum Beam Generation Based on a Dielectric Metasurface

Volume 12, Number 3, June 2020

Zhansong Lin
Zhongling Ba
Xiong Wang

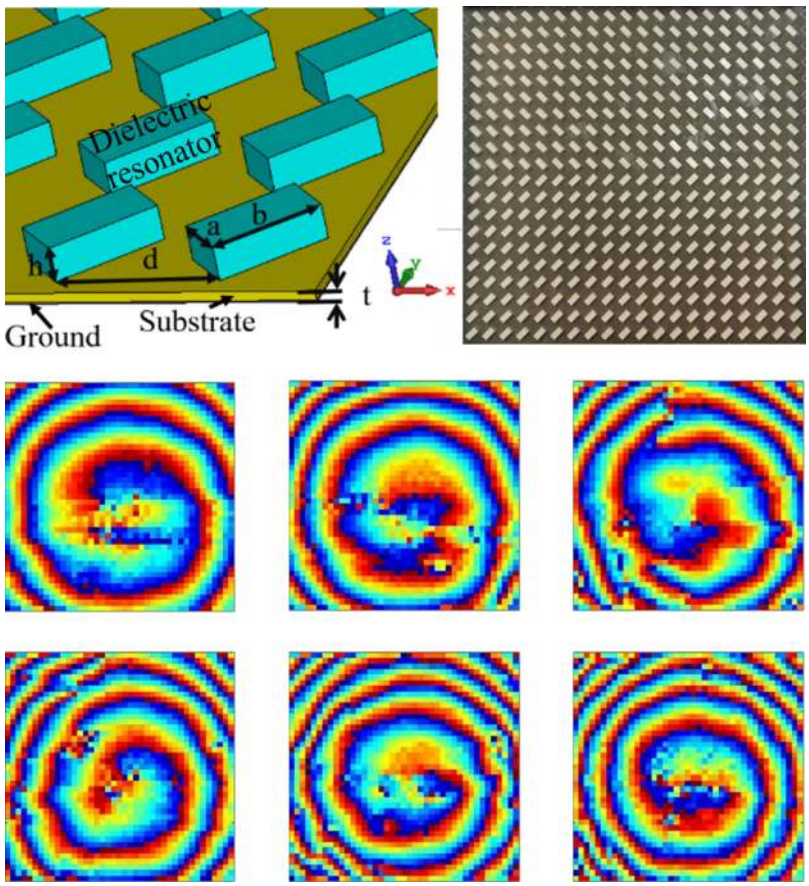

DOI: 10.1109/JPHOT.2020.2991114

Broadband High-Efficiency Electromagnetic Orbital Angular Momentum Beam Generation Based on a Dielectric Metasurface

Zhansong Lin,[1,2,3] Zhongling Ba,[1,2,3] and Xiong Wang[1,4]

[1]School of Information Science and Technology, ShanghaiTech University, Shanghai 201210, China
[2]Shanghai Institute of Microsystem and Information Technology, Chinese Academy of Sciences, Shanghai 200050, China
[3]University of Chinese Academy of Sciences, Beijing 100049, China
[4]Shanghai Engineering Research Center of Intelligent Vision and Imaging, Shanghai 201210, China

DOI:10.1109/JPHOT.2020.2991114

Manuscript received March 28, 2020; revised April 19, 2020; accepted April 24, 2020. Date of publication April 28, 2020; date of current version May 26, 2020. This work was supported in part by the National Natural Science Foundation of China under Grants 61701305, 61874073, and 61971287 and in part by the Open Project of State Key Laboratory of Millimeter Waves under Grant K201931.
Corresponding author: Xiong Wang (e-mail: wangxiong@shanghaitech.edu.cn).

Abstract: Electromagnetic waves carrying orbital angular momentum (OAM) have motivated a wealth of applications. Achromatic or broadband OAM beams are preferred in many applications and have been extensively explored in previous research endeavors. In view of the low efficiency of the previous reported broadband OAM generators, this work proposes a metasurface composed of high-refractive-index dielectric resonators to achieve broadband OAM beam generation with high efficiency. An efficient method for designing the resonators is presented, which indicates that proper adjustment of the dimensions and rotation of the dielectric resonators can render broadband and high-efficiency full phase control. A broadband high-efficiency OAM generator is engineered based on the resonators from 18 to 28 GHz as a proof-of-concept example and validated by both simulation and experiments. Above 70% polarization conversion efficiency and above 65% operation efficiency are measured throughout the entire design band. Such structure provides an alternative mechanism for realizing broadband high-efficiency microwave, millimeter-wave, terahertz or optical OAM generation and can find potential applications in high-capacity communications and imaging.

Index Terms: Orbital angular momentum (OAM), high efficiency, broadband, dielectric metasurface.

1. Introduction

Electromagnetic waves can carry both spin angular momentum and orbital angular momentum (OAM) [1]. The former pertains to polarization and the latter is associated with a helical or twisted wavefront [1]. OAM beams have witnessed a tremendous amount of research activities in the past two decades owing to their intriguing unconventional properties and exciting potential applications [2]–[7]. Theoretical investigation and exploration of diversified applications of OAM beams have been extensively reported first in the optical regime [8], where they are referred to optical vortex

beams, and subsequently in lower frequency domain like terahertz [9], millimeter wave [10], microwave [11] and radiofrequency band [12]. Among various novel applications of OAM beams, the capability of offering a brand-new mechanism of data multiplexing for high-capacity communications is probably the most fascinating one and has fueled widespread interests [13], [14].

An OAM beam is characterized with a helical wavefront described by an azimuthal phase dependence $e^{jm\varphi}$, where m is called the OAM mode number and φ represents the transverse azimuthal angle. A couple of approaches have been proposed to generate OAM beams with such azimuthal phase dependence in the microwave and millimeter wave range. The first way utilizes properly engineered structures like spiral phase plates [15]. The second technique makes use of circular waveguides [16]. The third one takes advantage of a phased array antenna with linearly varying excitation phases [17], [18]. The fourth method is based on metasurfaces [19], [20], which forms a spiral phase shift profile on the metasurface plates. A newly proposed technique makes use of the well-established transformation electromagnetics technique [21], [22]. Among these reported methods, the metasurface-based manner embraces obvious advantages against the other ones. For example, as a two-dimensional version of metamaterials, the metasurface generally has a subwavelength thickness rendering the associated OAM beam generators low-profile; while the spiral phase plates, circular waveguides and the devices based on transformation electromagnetics are intrinsically bulky and high-profile structures. Compared to the phased array OAM beam generators, the metasurface only requires a single excitation source, while the phased array demands many antenna elements and a complicated feeding network. In addition, the problems caused by the big divergence angle and air-dielectric mismatching inherent to the spiral phase plates OAM beam generators are significantly alleviated in the metasurface-based counterparts.

To accomplish successful applications of OAM beams in the microwave and millimeter wave regime, broad bandwidth and high efficiency are desired. Some techniques have been proposed to improve the bandwidth of OAM beams [23]–[26]. However, most of these broadband mechanisms are hindered by low power efficiency, i.e., operation efficiency. In addition, for some broadband OAM launching approaches equipped with the function of polarization conversion [24], [27], it is challenging to maintain favorable conversion efficiency throughout the entire design band. Although multilayer metasurfaces have been explored to enhance operation efficiency of the OAM beam generators [17], [24], the increased thickness in turn adds bulkiness and fabrication complexity to the structure. Therefore, there is a pressing need for a low-profile high-quality broadband OAM generator to improve the performance of relevant applications.

In this work, a reflection-type low-profile dielectric metasurface is proposed to engender linearly polarized microwave OAM beams with measured operation efficiency $>$65% and polarization conversion efficiency $>$70% over a broad frequency range from 18 to 28 GHz. The proposed metasurface is composed of different brick-shaped dielectric resonators with properly engineered dimensions and rotation angles situated on a grounded substrate. An efficient methodology for engineering the resonators is proposed and introduced in details. The designed resonators are then assembled and distributed in a specific manner to synthesize the metasurface for broadband high-efficiency OAM generation. Phase and amplitude profiles of the launched OAM beam are obtained both numerically and experimentally to demonstrate the effectiveness of the proposed design. Compared to previously reported microwave and millimeter-wave OAM generators, the most obvious superiority of the proposed dielectric metasurface is its high measured operation and conversion efficiency over the entire operation band. Although similar dielectric-resonator-based metasurfaces have been studied in the optical regime for the generation of OAM beams [28] this work is the first ever (to the best of the authors' knowledge) experimental demonstration of a microwave dielectric-resonator-based metasurface for broadband OAM beam generation. Compared with previous optical achromatic OAM generators making use of similar dielectric resonators, the design method of the proposed approach is easier and more efficient to be implemented. In addition, the $0.28\lambda_0$ thickness of the single-layer dielectric metasurface facilitates its realistic applications. The presented broadband high-efficiency OAM generator could be very useful for diversified applications and is possible to be scaled to other microwave or millimeter-wave frequency bands.

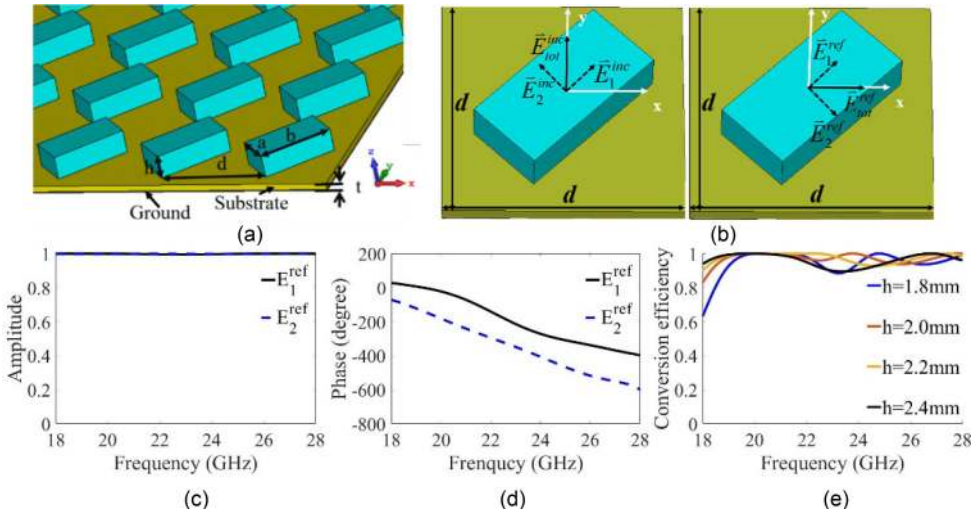

Fig. 1. (a) Schematic of the proposed dielectric metasurface. (b) Schematic explanation of the polarization conversion effect using a unit element. (c) and (d) are respectively the amplitudes (normalized) and phases of the reflected fields for the two electric field components in (b) using $a = 3.5$ mm, $b = 7$ mm, $d = 10$ mm, $h = 2.4$ mm, and $t = 0.6$ mm. (e) Simulated conversion efficiency of the first four unit elements having resonators with different heights.

2. Design Methodology

Metasurfaces are two-dimensional equivalents of metamaterials with thickness much smaller than a wavelength, which is thus endowed with the capability of introducing an abrupt phase change to the fields interfered with it and shaping the resultant wavefront in diversified manner [29]–[32]. Dielectric metasurfaces are applied in this work since they possess a favorable advantage over their metallic counterparts in terms of much less ohmic losses [33]. The dielectric metasurface structure is composed of high-refractive-index dielectric bricks situated on a low-refractive-index dielectric substrate, as depicted in Fig. 1(a). The substrate is backed by a ground plane, so this dielectric metasurface works in reflective mode that is easier to achieve high efficiency than the transmissive-mode metasurfaces [34]. Permittivity of the bricks is set to be 9.5, which can be implemented by commercially available ceramics. The substrate is implemented by the F4B material with dielectric constant of 2.65. Both materials are assumed to have negligible loss. Configuration of a unit element is showcased in Fig. 1(b). The high-refractive-index brick represents a good dielectric resonator that can support both electric and magnetic dipole responses, which are consequences of the Mie resonances [26]. Phase of the wave reflected by a unit element can be efficiently manipulated by tailoring the Mie resonances. Using a material with high refractive index can reduce the size of the brick resonators and enhance the sensitivity of phase control. However, smaller dielectric bricks are more challenging to fabricate. Thus, the chosen dielectric constant of the brick is a trade-off between the available commercial materials, associated fabrication complexity and performance of the broadband OAM beam.

Dimensions of the dielectric resonators are then designed to offer favorable phase and amplitude responses over the entire band from 18 to 28 GHz. The reflected fields E_{rx} and E_{ry} from a unit element can be related to incident fields E_{ix} and E_{iy} of a linearly polarized $-z$ propagating wave via a complex reflection matrix **R** given in (1) [35].

$$\begin{pmatrix} E_{rx} \\ E_{ry} \end{pmatrix} = \mathbf{R} \begin{pmatrix} E_{ix} \\ E_{iy} \end{pmatrix} = \begin{pmatrix} r_{xx} & r_{xy} \\ r_{yx} & r_{yy} \end{pmatrix} \begin{pmatrix} E_{ix} \\ E_{iy} \end{pmatrix} \tag{1}$$

To achieve 100% reflection efficiency, referred to as operation efficiency in this work, the dielectric resonator has to fulfill $|r_{xx}|^2 + |r_{yx}|^2 = 1$ and$|r_{xy}|^2 + |r_{yy}|^2 = 1$. One simple way satisfying this criterion is $r_{xx} = r_{yy} = 0$ and$r_{xy} = r_{yx} = 1$. This condition induces linear polarization conversion, i.e., the

reflected wave is cross-polarized with respect to the incident wave. Such polarization conversion can be accomplished by tilting the dielectric resonator by 45° with respect to the x and y axes defined in Fig. 1(a) and (b). To be specific, a y-polarized incident wave $\overrightarrow{E}_{tot}^{inc}$ can be decomposed into two electric field components $\overrightarrow{E}_{1}^{inc}$ and $\overrightarrow{E}_{2}^{inc}$ with equal amplitude, as depicted in Fig. 1(b). The resulting reflected fields of these two components are $\overrightarrow{E}_{1}^{ref}$ and $\overrightarrow{E}_{2}^{ref}$, respectively. Amplitude and phase of $\overrightarrow{E}_{1}^{ref}$ and $\overrightarrow{E}_{2}^{ref}$ are simulated by CST Microwave Studio using "Unit Cell" boundaries and results are shown in Fig. 1(c) and (d), exhibiting total reflectance and phase difference of π. Assuming $\overrightarrow{E}_{1}^{ref}$ maintains the same polarization as $\overrightarrow{E}_{1}^{inc}$, then $\overrightarrow{E}_{2}^{ref}$ is reversed in polarization as compared to $\overrightarrow{E}_{2}^{inc}$ due to the π phase difference. Accordingly, $\overrightarrow{E}_{1}^{ref}$ and $\overrightarrow{E}_{2}^{ref}$effectively form an x-polarized reflected wave and realize the polarization conversion.

In order to control the phase response of the dielectric resonator, there are two options have been investigated in literature, namely rotating the resonator and changing the dimensions of the resonator. If the dielectric resonator is azimuthally rotated by an angle of α in the xy plane, the new reflection matrix $\mathbf{R}(\alpha)$ under the condition of $r_{xx} = r_{yy} = 0$ and $r_{xy} = r_{yx} = 1$ is described in (2), which reveals the rotation-angle-dependent phase control mechanism [35], [36].

$$\mathbf{R}(\alpha) = \begin{pmatrix} -\sin(2\alpha) & \cos(2\alpha) \\ \cos(2\alpha) & \sin(2\alpha) \end{pmatrix} \tag{2}$$

After performing some preliminary simulation studies, it has been found that combining rotation and dimension adjustment can greatly simplify the design procedure. To be specific, phase control θ within $(0, \pi]$ is obtained by appropriately tuning the dimensions of the resonator in the configuration in Fig. 1(b). For phase control values falling into the range of $\pi < \theta \leq 2\pi$, they can be readily realized by azimuthally rotating the resonators for the $0 < \theta \leq \pi$ cases by 90° since $\mathbf{R}(90°) = -\mathbf{R}(0°)$. Furthermore, the full phase control from 0 to 2π in the targeted frequency range from 18 to 28 GHz is implemented by eight discrete values from $\pi/4$ to 2π with a step of $\pi/4$ to simplify the design. The first four phase values are realized by four resonators (denoted as resonator 1, 2, 3 and 4) with properly engineered dimensions and the rest four (denoted as resonator 5, 6, 7 and 8) are achieved via rotation of the first four resonators. What needs to be emphasized is that the main objective of the resonator design is to figure out dimensions of the first four resonators that enable all the eight resonators to exhibit high operation efficiency and linearly varying phase shift featured by an incremental phase around $\pi/4$ at each frequency point in the 18 to 28 GHz band. Although the phase response induced by each resonator cannot keep unchanged if frequency is varied, which renders broadband phase manipulation seemingly impossible, maintaining a largely unchanged phase increment between the eight resonators is accessible and sufficient for relevant broadband applications exercising the resonator-based dielectric metasurface.

Based on the established design recipes above, dimensions of the dielectric resonators and thickness of the substrate are tuned via the optimization function in CST. A linearly polarized $-z$ propagating plane wave is applied to irradiate the unit element containing the resonator and grounded substrate. Period of the unit element is chosen as $d = 10$ mm, which is smaller than a wavelength in the entire design bandwidth. To further facilitate the realistic fabrication of the dielectric resonators, only the height of the resonator is varied in the optimization process. By this manner, the parameters to be optimized and total time consumed for optimization is reduced, which renders the design method less complicated and more efficient than the cases demanding variation in two or three dimensions of the resonators to tune the phase [27]. The optimal width and length of the resonator and thickness of the substrate are found to be $a = 3.5$ mm, $b = 7$ mm and $t = 0.6$ mm, respectively. The obtained optimal heights h for all the eight resonators are listed in Table 1.

Simulated conversion efficiency of the first four elements is shown in Fig. 1(e), which is defined as,

$$\eta_c = \frac{|E_{cross}|^2}{|E_{cross}|^2 + |E_{co}|^2} \times 100\% \tag{3}$$

TABLE 1
Optimized Height of Dielectric Resonators

Resonator number	1	2	3	4	5	6	7	8
Resonator height (mm)	2.4	2.2	2.0	1.8	2.4	2.2	2.0	1.8
Rotation angle (degree)	0	0	0	0	90	90	90	90
Targeted phase response	$\pi/4$	$\pi/2$	$3\pi/4$	π	$5\pi/4$	$3\pi/2$	$7\pi/4$	2π

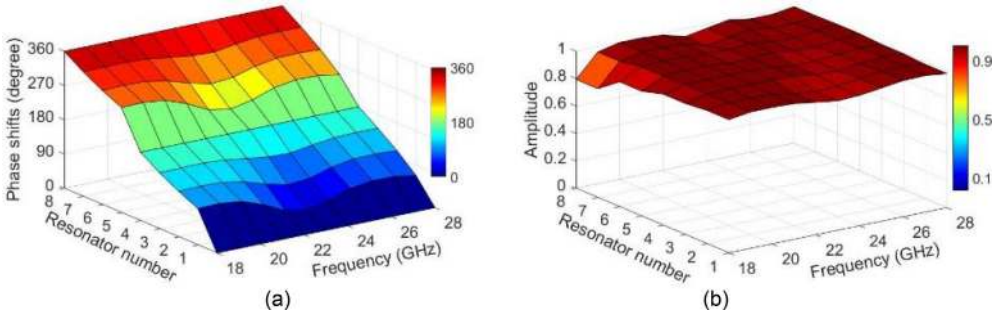

Fig. 2. Simulated phase responses (a) and amplitude responses (b) of cross-polarized reflected waves for the eight resonators.

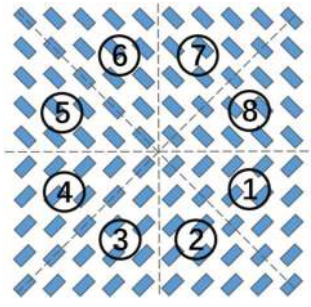

Fig. 3. Schematic of metasurface-based OAM generator. Section *n* is filled with resonator *n*.

where E_{cross} and E_{co} denote cross- and co-polarized reflected electric field components. It is apparent that the conversion efficiency maintains over 0.9 for most of the bandwidth. Although it is relatively low for the 1.8-mm-high resonator around 18 GHz, the average conversion efficiency at 18 GHz is still higher than 82.5%. Degradation in the conversion efficiency is mainly because the phase difference between the two orthogonal polarizations is not exactly π. Simulated phase responses of the cross-polarized reflected waves for the eight resonators are plotted in Fig. 2(a) as a function of frequency. It is obvious that the phase increases from resonator 1 to 8 with an incremental phase of approximately $\pi/4$ in the entire bandwidth. The corresponding amplitude of the cross-polarized reflected waves is also showcased in Fig. 2(b). All the resonators present an over 80% reflectance across the design bandwidth. Therefore, both the phases and amplitudes of all the designed dielectric resonators satisfy the requirement for a broadband OAM generator.

An OAM generator with mode number $m = -1$ is subsequently designed using the optimized eight resonators as an example to validate the proposed design methodology based on the dielectric metasurface. The phase profile for this OAM beam, assumed to be propagating in the $+z$ axis, decreases counterclockwise (along the azimuthal direction) from 2π to 0 in the *xy* plane. To realize such a phase distribution, a metasurface plate is divided into eight sections (denoted as section 1 to 8) and section *n* is filled with resonator *n*, as shown in Fig. 3. As a result, the phase

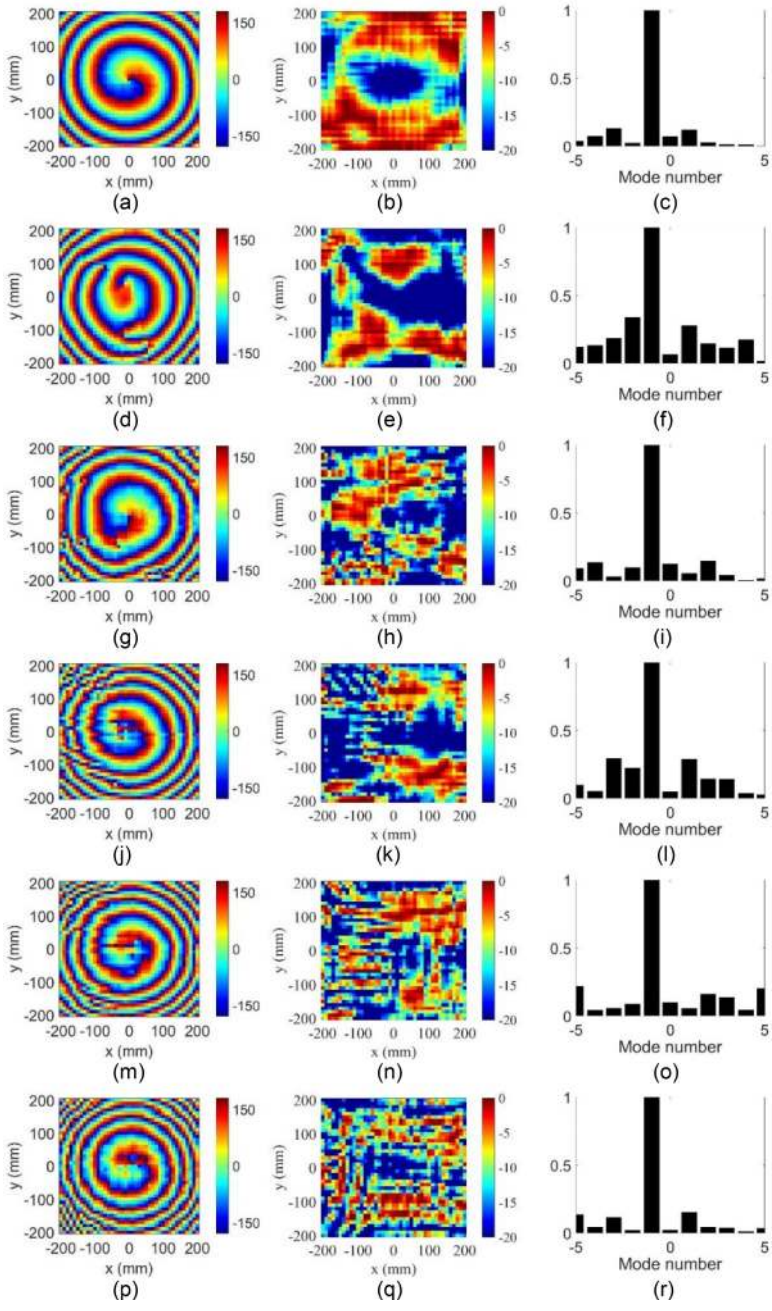

Fig. 4. Simulated phase profiles (in degree), normalized amplitude profiles (in dB scale), and mode spectra of the cross-polarized electric fields of the generated $m = -1$ OAM beam at 18 GHz (a)–(c), 20 GHz (d)–(f), 22 GHz (g)–(i), and 24 GHz (j)–(l), 26 GHz (m)–(o) and 28 GHz (p)–(r).

differences between each two adjacent sections are kept at $-\pi/4$ and 2π to 0 phase variation can be achieved in a stepped manner along the azimuthal direction.

3. Simulation Results

A complete reflective dielectric metasurface plate consisting of 40 $\times$ 40 elements is simulated in CST ("Open" boundaries are used) to visualize the generation of broadband OAM beams. A circular

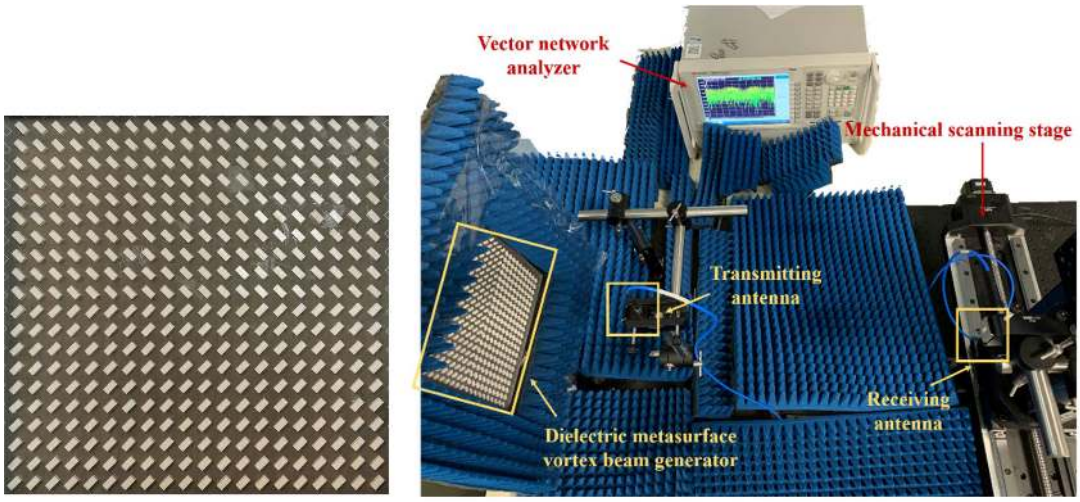

Fig. 5. (a) Photo of the fabricated dielectric metasurface. (b) Setup of the experiment.

waveguide located on the z axis and 150 mm from the plate serves as a feeding antenna. Simulated phase profiles of the cross-polarized reflected electric fields 400 mm away from the metasurface plate at different frequencies are provided in Fig. 4, which unambiguously manifest the broadband spiral phase nature for an OAM beam with $m = -1$. For the simulated amplitude results, doughnut-shaped patterns can be observed at all the simulated frequencies. To quantitatively evaluate quality of the OAM beams, OAM mode spectra [37] are also calculated and shown in Fig. 4, from which it is seen that the mode $m = -1$ is predominant throughout the design frequency band. The calculated mode purity is higher than 0.75 across the entire bandwidth and exhibits an average value of 0.85. The imperfection in the mode purity is mainly caused by the nonlinearity in the phase variation of the eight designed resonators, as shown in Fig. 2(a).

4. Experimental Results

To experimentally verify the performance of the designed broadband dielectric OAM generator, a metasurface plate including 20 $\times$ 20 unit elements, occupying a dimension of 200 mm $\times$ 200 mm, is manufactured on a 0.6-mm-thick F4B (dielectric constant is 2.65 and loss tangent is 0.001) printed circuit board. The dielectric resonators are made of commercially available ceramic material with dielectric constant of 9.5 and loss tangent of 0.0009 (Premix, PREPERM PPE950) and cut to the designed dimensions by a carving machine. Photograph of the fabricated metasurface is provided in Fig. 5(a), in which the while rectangles are the ceramic dielectric resonators. The commonly applied near-field scanning approach is utilized to characterize the launched OAM beam. As shown in the experimental setup in Fig. 5(b), both transmitting and receiving antennas are linear-polarized WR-42 rectangular waveguide antennas carrying the dominant mode TE_{10}. The transmitting antenna and the metasurface plate are separated by 150 mm. The receiving antenna detects the reflected microwave signal and is mounted on a mechanical scanning stage to conduct near-field scanning in a 400 mm $\times$ 400 mm *xy* region with a step of 10 mm. The scanning is performed in a plane parallel to and 600 mm away from the plate. The transmitting antenna is configured to radiate vertically polarized wave to the plate while the receiving antenna is set to harvest horizontally polarized wave. The two antennas are connected by a vector network analyzer (Keysight technologies, N5227A) and the scattering parameter S_{21} is measured from 18 to 28 GHz.

The measured phase and amplitude results are shown in Figs. 6. It is apparently observed that the phase distributions at all the frequencies present high-quality spiral feature associated with a

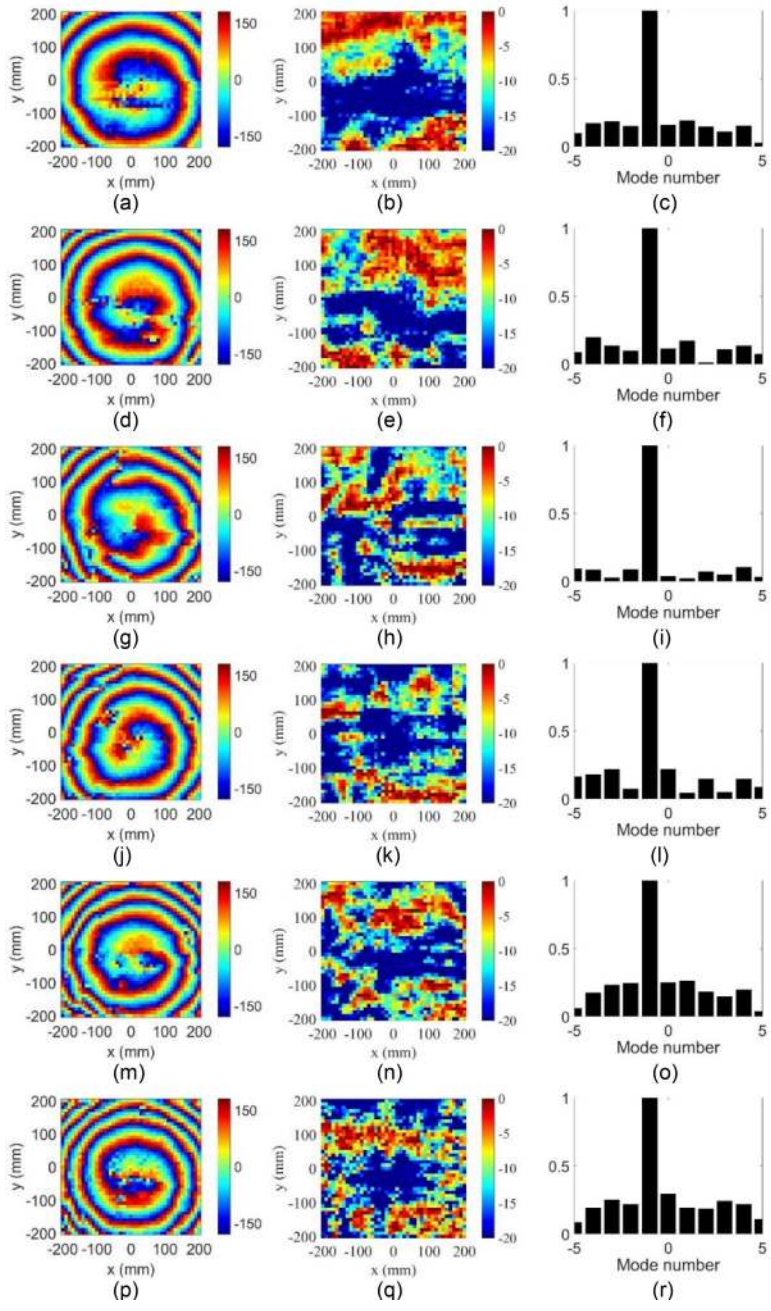

Fig. 6. Measured phase profiles (in degree), normalized amplitude profiles (in dB scale), and mode spectra of the cross-polarized electric fields of the generated $m = -1$ OAM beam at 18 GHz (a)–(c), 20 GHz (d)–(f), 22 GHz (g)–(i), 24 GHz (j)–(l), 26 GHz (m)–(o) and 28 GHz (p)–(r).

$m = -1$ OAM beam. The corresponding amplitude profiles have a doughnut-shaped pattern. It is also perceived that the measurement results show a good agreement between different frequencies, which proves the broadband nature of the proposed OAM generator. The obtained mode spectra also corroborate the high quality of the generated OAM beam as the $m = -1$ mode possesses overwhelming magnitude compared to all the other modes. The obtained mode purity for the measured results is higher than 0.65 across the entire bandwidth and has an average value of 0.81. Some deficiencies in the measured results are probably attributed to two reasons. First, partial

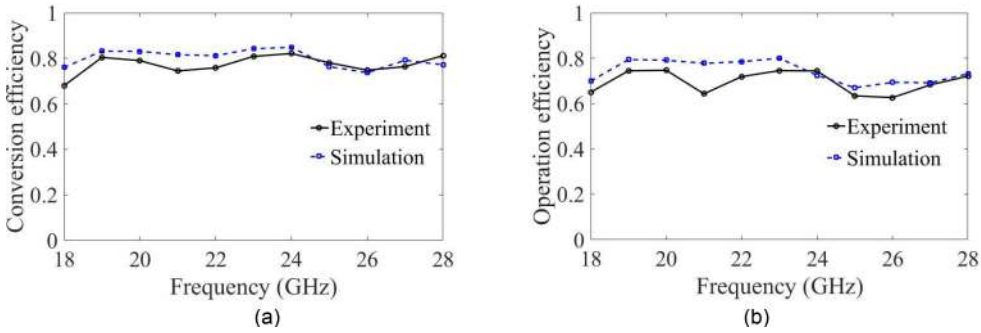

Fig. 7. Conversion efficiency (a) and operation efficiency (b) of the simulated and measured OAM beam.

TABLE 2
Comparison With Previous Works in Terms of Key Parameters

Key parameter	Bandwidth (fractional bandwidth)	Conversion efficiency	Operation efficiency	Mode of operation
Ref. [17]	9.6-10.4 GHz (10.0%)	>49%	>16%	Transmission
Ref.[20]	8-16 GHz (66.7%)	NA	NA	Reflection
Ref. [23]	2.1-2.7 GHz (25.0%)	NA	NA	Transmission
Ref. [24]	7.5-10.5 GHz (33.3%)	>45%	>35%	Transmission
Ref.[25]	4.9-6.5 GHz (28.1%)	NA	NA	Reflection
Ref.[27]	9.3-10.3 GHz (10.2%)	NA	>75%	Transmission
Ref. [37]	59-70 GHz (17.1%)	>64%	NA	Reflection
Ref. [38]	10-30 GHz (100.0%)	NA	>20%	Transmission/ Reflection
Ref. [39]	28-37.3 GHz (28.5%)	NA	NA	Transmission
Ref.[40]	9.5-10.5 GHz (10.0%)	NA	NA	Transmission
Ref. [41]	13-15 GHz (14.2%)	NA	NA	Transmission
Ref. [42]	9-11 GHz (20.0%)	NA	>72%	Transmission
Ref. [43]	532-780 nm (37.8%)	>23%	NA	Transmission
Ref. [44]	760-790 nm (3.9%)	>8.2%	NA	Transmission
This work	18-28 GHz (43.5%)	>70%	>65%	Reflection

reflected wave is blocked and scattered by the transmitting antenna and its feeding cable, which distorts the recorded phase and amplitude distributions. Second, some errors are unavoidable in the fabrication procedure, such as deviations in the dimensions of the ceramic resonators (about $\pm$0.02 mm) and the losses in the materials as well as the silicone gel used to paste the resonators on the substrate.

Conversion efficiency of the OAM beam generator is calculated and plotted in Fig. 7(a), which is higher than 70% over the entire band. The operation efficiency is also given in Fig. 7(b), which is defined as

$$\eta_o = \frac{\int \vec{E}_r \times \vec{H}_r^* ds}{\int \vec{E}_i \times \vec{H}_i^* ds} \times 100\% = \frac{\int \vec{E}_r \times \vec{H}_r^* ds}{\int \vec{E}_{pec} \times \vec{H}_{pec}^* ds} \times 100\%, \quad (4)$$

where $\vec{E}_r$ and $\vec{H}_r$ are respectively the measured reflected electric and magnetic fields, $\vec{E}_i$ and $\vec{H}_i$ are respectively the incident electric and magnetic field, and $\vec{E}_{pec}$ and $\vec{H}_{pec}$ are respectively the measured reflected electric and magnetic fields with the metasurface replaced by a PEC plane. It is seen that the average operation efficiency in the whole band is 70%. The operation efficiency is expected to be further improved if the measurements are done in a bigger area.

A detailed comparison between this work and previous reported broadband OAM generators in terms of several key parameters is given in Table 2. Only experimentally measured efficiencies are considered here. The lowest conversion efficiency and operation efficiency are used for the comparison since the lower limit of a parameter is generally the adopted criterion for defining the related bandwidth. It is unambiguously demonstrated that this work is more advantageous than the previous research works in terms of bandwidth, conversion efficiency and operation efficiency. Even if a few works ([27], [42]) exhibit a little higher operation efficiency than this work, the bandwidth of this work is significantly wider than these works.

5. Conclusion

A broadband 18–28 GHz high-efficiency microwave OAM generator based on dielectric metasurface is proposed in this work. The metasurface is made of high-refractive-index brick-shaped dielectric resonators with properly designed dimensions. The underlying working principle and efficient design method of the resonators are presented. Linearly varying full phase control with high efficiency is obtained by eight resonators with optimized dimensions. Satisfactory quality of the generated OAM beams is validated by simulation and experimental results in the entire design bandwidth, including phase profiles, amplitude patterns and mode spectra. Measured conversion and operation efficiency compare favorably with those previous broadband OAM generators, further corroborating the effectiveness of the proposed technique. The proposed technique can also be applied to produce higher-order OAM beams [45]. This work may be useful in microwave, millimeter-wave, terahertz and optical OAM involved applications.

References

[1] L. Allen, M. W. Beijersbergen, R. Spreeuw, and J. Woerdman, "Orbital angular momentum of light and the transformation of Laguerre-Gaussian laser modes," *Phys. Rev. A*, vol. 45, no. 11, 1992, Art. no. 8185.
[2] W. Pan, L. Xu, J. Li, and X. Liang, "Generation of high-purity Laguerre–Gaussian beams by spatial filtering," *IEEE Photon. J.*, vol. 11, no. 3, Jun. 2019, Art. no. 1502310.
[3] Y. L. He *et al.*, "Order-controllable cylindrical vector vortex beam generation by using spatial light modulator and cascaded metasurfaces," *IEEE Photon. J.*, vol. 9, no. 5, 2017, Art. no. 6101710.
[4] Z. Q. Xin, C. L. Zhang, and X. C. Yuan, "Concentric perfect optical vortex beam generated by a digital micromirrors device," *IEEE Photon. J.*, vol. 9, no. 2, 2017, Art. no. 7903107.
[5] Y. Zhang *et al.*, "Generation of the first-order OAM modes in ring fibers by exerting pressure technology," *IEEE Photon. J.*, vol. 9, no. 2, Oct. 2017, Art. no. 7101609.
[6] Z. Y. Guo, Z. K. Wang, M. I. Dedo, and K. Guo, "The orbital angular momentum encoding system with radial indices of laguerre-gaussian beam," *IEEE Photon. J.*, vol. 10, no. 5, 2018, Art. no. 7906511.
[7] S. H. Li, Z. Xu, R. X. Zhao, L. Shen, C. Du, and J. Wang, "Generation of orbital angular momentum beam using fiber-to-fiber butt coupling," *IEEE Photon. J.*, vol. 10, no. 4, 2018, Art. no. 6601607.
[8] P. Genevet, *et al.*, "Ultra-thin plasmonic optical vortex plate based on phase discontinuities," *Appl. Phys. Lett.*, vol. 100, no. 1, 2012, Art. no. 013101.
[9] Z. Chang, B. You, L.-S. Wu, M. Tang, Y.-P. Zhang, and J.-F. Mao, "A reconfigurable graphene reflectarray for generation of vortex THz waves," *IEEE Antennas Wirel. Propag. Lett.*, vol. 15, pp. 1537–1540, 2016.
[10] L. Cheng, W. Hong, and Z.-C. Hao, "Generation of electromagnetic waves with arbitrary orbital angular momentum modes," *Sci. Rep.*, vol. 4, no. 1, pp. 1–5, 2014.
[11] K. Liu, *et al.*, "Generation of OAM beams using phased array in the microwave band," *IEEE Trans. Antennas Propag.*, vol. 64, no. 9, pp. 3850–3857, 2016.
[12] T. Yuan, Y. Cheng, H.-Q. Wang, and Y. Qin, "Generation of OAM radio beams with modified uniform circular array antenna," *Electron. Lett.*, vol. 52, no. 11, pp. 896–898, 2016.
[13] T. L. Wang, J. A. Gariano, and I. B. Djordjevic, "Employing Bessel-Gaussian beams improve physical-layer security in free-space optical communications," *IEEE Photon. J.*, vol. 10, no. 5, 2018, Art. no. 7907113.
[14] Y. Yan *et al.*, "High-capacity millimetre-wave communications with orbital angular momentum multiplexing," *Nature Commun.*, vol. 5, no. 1, pp. 1–9, 2014.

[15] X. Hui, S. Zheng, Y. Hu, C. Xu, X. Jin, H. Chi, and X. Zhang, "Ultralow reflectivity spiral phase plate for generation of millimeter-wave OAM beam," *IEEE Antennas Wirel. Propag. Lett.*, vol. 14, pp. 966–969, 2015.
[16] X. Bai, X. Liang, R. Jin, and J. Geng, "Generation of OAM radio waves with three polarizations using circular horn antenna array," in *Proc. 9th Eur. Conf. Antennas Propag.*, 2015, pp. 1–4.
[17] Y. Meng, J. Yi, S. N. Burokur, L. Kang, H. Zhang, and D. H. Werner, "Phase-modulation based transmitarray convergence lens for vortex wave carrying orbital angular momentum," *Opt. Express*, vol. 26, no. 17, pp. 22019–22029, 2018.
[18] K. Bi, J. C. Xu, D. Q. Yang, Y. N. Hao, X. L. Gao, and S. G. Huang, "Generation of orbital angular momentum beam with circular polarization ceramic antenna array," *IEEE Photon. J.*, vol. 11, no. 2, 2019, Art. no. 7901508.
[19] S. Yu, L. Li, G. Shi, C. Zhu, X. Zhou, and Y. Shi, "Design, fabrication, and measurement of reflective metasurface for orbital angular momentum vortex wave in radio frequency domain," *Appl. Phys. Lett.*, vol. 108, no. 12, 2016, Art. no. 121903.
[20] J. J. Jin, X. Li, M. B. Pu, X. L. Ma, and X. G. Luo, "Wavelength-dependent three-dimensional volumetric optical vortices modulation based on metasurface," *IEEE Photon. J.*, vol. 11, no. 2, 2019, Art. no. 4502008.
[21] J. Yi *et al.*, "All-dielectric transformed material for microwave broadband orbital angular momentum vortex beam," *Phys. Rev. Appl.*, vol. 10, no. 6, 2018, Art. no. 024064.
[22] R. Feng, J. Yi, S. N. Burokur, L. Kang, H. Zhang, and D. H. Werner, "Orbital angular momentum generation method based on transformation electromagnetics," *Opt. Express*, vol. 26, no. 9, pp. 11708–11717, 2018.
[23] B. Liu, Y. Cui, and R. Li, "A broadband dual-polarized dual-OAM-mode antenna array for OAM communication," *IEEE Antennas Wireless Propag. Lett.*, vol. 16, pp. 744–747, 2016.
[24] S. Jiang, C. Chen, H. Zhang, and W. Chen, "Achromatic electromagnetic metasurface for generating a vortex wave with orbital angular momentum (OAM)," *Opt. Express*, vol. 26, no. 5, pp. 6466–6477, 2018.
[25] J. Wu, Z. Zhang, X. Ren, Z. Huang, and X. Wu, "A broadband electronically mode-reconfigurable orbital angular momentum metasurface antenna," *IEEE Antennas Wirel. Propag. Lett.*, vol. 18, no. 7, pp. 1482–1486, 2019.
[26] F. Mao, M. Huang, T. Li, J. Zhang, and C. Yang, "Broadband generation of orbital angular momentum carrying beams in RF regimes," *Prog. Electromagnetics Res.*, vol. 160, pp. 19–27, 2017.
[27] K. Zhang *et al.*, "Phase-engineered metalenses to generate converging and non-diffractive vortex beam carrying orbital angular momentum in microwave region," *Opt. Express*, vol. 26, no. 2, pp. 1351–1360, 2018.
[28] Y. Yang, W. Wang, P. Moitra, I. I. Kravchenko, D. P. Briggs, and J. Valentine, "Dielectric meta-reflectarray for broadband linear polarization conversion and optical vortex generation," *Nano Lett.*, vol. 14, no. 3, pp. 1394–1399, 2014.
[29] N. Yu *et al.*, "Light propagation with phase discontinuities: Generalized laws of reflection and refraction," *Science*, vol. 334, no. 6054, pp. 333–337, 2011.
[30] R. Xie, G. Zhai, X. Wang, D. Zhang, L. Si, H. Zhang, and J. Ding, "High-efficiency ultrathin dual-wavelength pancharatnam–berry metasurfaces with complete independent phase control," *Adv. Opt. Mater.*, vol. 7, no. 20, 2019, Art. no. 1900594.
[31] J. Ding, S. An, B. Zheng, and H. Zhang, "Multiwavelength metasurfaces based on single-layer dual-wavelength meta-atoms: Toward complete phase and amplitude modulations at two wavelengths," *Adv. Opt. Mater.*, vol. 5, no. 10, 2017, Art. no. 1700079.
[32] F. H. Lin and Z. N. Chen, "Low-profile wideband metasurface antennas using characteristic mode analysis," *IEEE Trans. Antennas Propag.*, vol. 65, no. 4, pp. 1706–1713, 2017.
[33] Y. F. Yu, A. Y. Zhu, R. Paniagua-Domínguez, Y. H. Fu, B. Luk'yanchuk, and A. I. Kuznetsov, "High-transmission dielectric metasurface with 2π; phase control at visible wavelengths," *Laser Photon. Rev.*, vol. 9, no. 4, pp. 412–418, 2015.
[34] M. R. Akram, M. Q. Mehmood, X. Bai, R. Jin, M. Premaratne, and W. Zhu, "High efficiency ultrathin transmissive metasurfaces," *Adv. Opt. Mater.*, vol. 7, no. 11, 2019, Art. no. 1801628.
[35] C. Menzel, C. Rockstuhl, and F. Lederer, "Advanced Jones calculus for the classification of periodic metamaterials," *Phys. Rev. A*, vol. 82, no. 5, 2010, Art. no. 053811.
[36] M. R. Akram, X. Bai, R. Jin, G. A. Vandenbosch, M. Premaratne, and W. Zhu, "Photon spin Hall effect-based ultra-thin transmissive metasurface for efficient generation of OAM waves," *IEEE Trans. Antennas Propag.*, vol. 67, no. 7, pp. 4650–4658, 2019.
[37] F. Bi, Z. Ba, and X. Wang, "Metasurface-based broadband orbital angular momentum generator in millimeter wave region," *Opt. Express*, vol. 26, no. 20, pp. 25693–25705, 2018.
[38] M. R. Akram, G. Ding, K. Chen, Y. Feng, and W. Zhu, "Ultrathin single layer metasurfaces with ultra-wideband operation for both transmission and reflection," *Adv. Mater.*, 2020, Art. no. 1907308.
[39] R. Niemiec, C. Brousseau, K. Mahdjoubi, O. Emile, and A. Ménard, "Characterization of an OAM flat-plate antenna in the millimeter frequency band," *IEEE Antennas Wirel. Propag. Lett.*, vol. 26, no. 20, pp. 25693–25705, 2018.
[40] L. Ma, C. Chen, L. Zhou, S. Jiang, and H. Zhang, "Single-layer transmissive metasurface for generating OAM vortex wave with homogeneous radiation based on the principle of Fabry-Perot cavity," *Appl. Phys. Lett.*, vol. 114, no. 8, 2019, Art. no. 081603.
[41] F. Qin, S. Gao, W.-C. Cheng, Y. Liu, H.-L. Zhang, and G. Wei, "A high-gain transmitarray for generating dual-mode OAM beams," *IEEE Access*, vol. 6, pp. 61006–61013, 2018.
[42] F. Zhang, Q. Song, G.-M. Yang, and Y.-Q. Jin, "Generation of wideband vortex beam with different OAM modes using third-order meta-frequency selective surface," *Opt. Express*, vol. 27, no. 24, pp. 34864-3-4875, 2019.
[43] M. Pu *et al.*, "Catenary optics for achromatic generation of perfect optical angular momentum," *Sci. Adv.*, vol. 1, no. 9, 2015, Art. no. e1500396.
[44] F. Bouchard, I. De Leon, S. A. Schulz, J. Upham, E. Karimi, and R. W. Boyd, "Optical spin-to-orbital angular momentum conversion in ultra-thin metasurfaces with arbitrary topological charges," *Appl. Phys. Lett.*, vol. 105, no. 10, 2014, Art. no. 101905.
[45] Z. Ba and X. Wang, "Metasurface for generating high-order millimeter wave orbital angular momentum beams," in *Proc. Int. Appl. Comput. Electromagn. Soc. Symp.*, Beijing, China, 2018, pp. 1–2.